

RESEARCH ARTICLE

10.1029/2019GC008692

Special Section:

Magmatic and volcanic processes
in continental rifts

Key Points:

- A fissure on the south flank of Erta 'Ale began erupting on 21 January 2017 and has remained active until at least July 2019
- We observe and model ground deformation and lava lake levels in the buildup to and during the eruption using synthetic aperture radar
- We suggest that below a shallow reservoir, melt may be stored in a vertically extensive off-rift system

Supporting Information:

- Supporting Information S1

Correspondence to:

C. Moore,
ee12cm@leeds.ac.uk

Citation:

Moore, C., Wright, T., Hooper, A., & Biggs, J. (2019). The 2017 eruption of Erta 'Ale Volcano, Ethiopia: Insights into the shallow axial plumbing system of an incipient mid-ocean ridge. *Geochemistry, Geophysics, Geosystems*, 20, 5727–5743. <https://doi.org/10.1029/2019GC008692>

Received 10 SEP 2019

Accepted 16 NOV 2019

Accepted article online 23 NOV 2019

Published online 03 DEC 2019

The 2017 Eruption of Erta 'Ale Volcano, Ethiopia: Insights Into the Shallow Axial Plumbing System of an Incipient Mid-Ocean Ridge

C. Moore¹ , T. Wright¹ , A. Hooper¹ , and J. Biggs² 

¹COMET, School of Earth and Environment, University of Leeds, Leeds, UK, ²COMET, School of Earth Sciences, University of Bristol, Bristol, UK

Abstract The final stage of continental breakup is often accompanied by abundant magmatism. Erta 'Ale volcano lies on the Nubia-Arabia extensional boundary in Afar, Ethiopia, an incipient mid-ocean ridge. A fissure on the south flank of Erta 'Ale began erupting on 21 January 2017 and has remained active until at least July 2019. We use Sentinel-1 synthetic aperture radar acquisitions to create a time series of ground displacement measurements at Erta 'Ale from October 2014 to June 2019, covering the eruption and its buildup. In the preeruption period, we observe gradual extension centered on the lava lake, consistent with the opening of an axis-aligned dike. Using synthetic aperture radar intensity shadows, we show that the long-lived Erta 'Ale lava lake was stable in this period, indicative of a steady pressure state in the shallow plumbing system. During the initial eruption, we observe surface displacements consistent with a shallow dike intrusion below the eruption site and conduit contraction below the lava lake. The pressure change associated with the cointrusive drop in the lava lake level is sufficient to reproduce the deformation pattern suggesting that the lava lake is well connected to the shallow plumbing system. Subsidence and contraction during the long-lived eruption indicates the presence of an off-rift vertically extensive source. We suggest that this may represent a system of stacked sources throughout the upper crust, with melt being more distributed. We also propose that high magma flux on the slow-spreading Erta 'Ale segment may be facilitating the presence of shallow axial magma bodies.

1. Introduction

The geometry and dynamics of magma plumbing systems at subaerial volcanoes in extensional settings are still poorly understood (Pagli et al., 2012; Sigmundsson, 2016; Wright et al., 2012). Extensive studies on mid-ocean ridge (MOR) systems show that at fast-spreading ridges, a shallow sill structure is commonly found (Carbotte et al., 2013; Marjanović et al., 2014; Wanless & Behn, 2017). For example, at the East Pacific Rise (EPR) from 8°20' to 10°10'N, an axial magma lens is typically present at ~1.6 km depth, with a deeper lens found between ~1.7 and 2.4 km depth (Carbotte et al., 2013; Marjanović et al., 2018). While fast-spreading MOR plumbing systems are well imaged, the movement of magma and dynamics within these plumbing systems are difficult to study (Sigmundsson, 2016). The slow-spreading Erta 'Ale volcanic segment (EAVS) in northern Afar, Ethiopia (Figure 1a), represents the southern end of the Red Sea Rift (RSR) and has been previously proposed as a subaerial analog for a MOR (e.g., Ebinger, 2005). Although the spreading rate is low (5–15 mm/year) (McClusky et al., 2010), the EAVS exhibits features typical of a fast-spreading MOR such as a broad axial ridge (Barberi & Varet, 1970), the presence of a shallow axial magma chambers below the EAVS (e.g., Pagli et al., 2012), and the formation of a proto-transform fault between the Erta 'Ale and Tat 'Ale segments (Illsley-Kemp et al., 2018b). Understanding the dynamics of magma movement at the EAVS can therefore give us insights into magma plumbing systems at fast-spreading MORs.

Erta 'Ale volcano lies at the southern end of the EAVS and is host to one of the few long-lived lava lakes in the world. The lava lake overflowed in January 2017, before a large fissure eruption ~3 km to its SE (Global Volcanism Program, 2017). The eruption has remained active until at least June 2019. At Kilauea volcano, Hawaii, the interaction between the summit Halema'uma'u lava lake and the established Pu'u 'O'o vent in the East Rift Zone on the volcano flank has highlighted a strong interconnectivity in its shallow plumbing system (Montagna & Gonnermann, 2013; Neal et al., 2019; Patrick et al., 2019a, 2019b), with long-term fluctuations in the lava lake level giving an indication of the pressure state of the summit reservoir and the

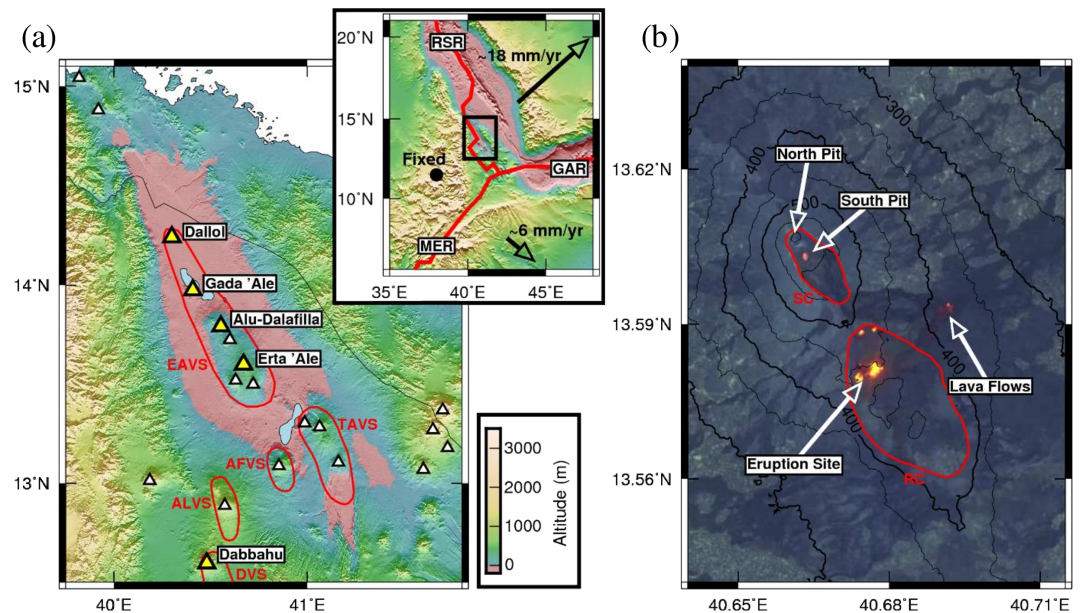


Figure 1. (a) The Danakil depression in northern Afar with Holocene volcano locations from the Smithsonian Institute Global Volcanism Program marked as white triangles and key volcanoes highlighted in yellow. Simplified volcanic segments (VS) (Wolfenden et al., 2005) are shown in red: EAVS = Erta 'Ale; TAVS = Tat 'Ale; AFVS = Afdera; ALVS = Alayta; DVS = Dabbahu. Inset map shows the relative movement of the Arabian and Somalian plates to the Nubian plate, with plate boundaries from (Bird, 2003). RSR = Red Sea Rift; GAR = Gulf of Aden Rift; MER = Main Ethiopian Rift. Region shown in (a) is outlined in black. (b) ESA Sentinel-2 false-color optical image (Bands 12, 11, and 4) of Erta 'Ale volcano on 8 February 2017, with elevation contours, and the summit (SC) and relic (RC) calderas outlined in red. Areas of high thermal output from the eruption site, lava lake, and fresh lava flows are shown as bright red/orange (from short-wave infrared bands).

balance between magma influx and out-flux (Anderson et al., 2015; Patrick et al., 2015, 2019b). The 2017 Erta 'Ale flank eruption, and potential connectivity with the lava lake, provides a similar opportunity to understand the pressure state of the shallow plumbing system at Erta 'Ale.

1.1. Tectonic Setting

The ~120 km long EAVS forms part of the RSR branch of the Afar triple junction, which initiated ~30 Ma, and accommodates the separation of the Nubian, Somalian, and Arabian plates (Wolfenden et al., 2005) (Figure 1a). Extension over the RSR of ~18 mm/year is gradually transferred into Afar between ~13° and 16°N which produces an extension of ~12 mm/year at Erta 'Ale (ArRajehi et al., 2010; McClusky et al., 2010; Pagli et al., 2014). The EAVS lies within the Danakil Depression, which has the most thinned crustal structure in Afar with a thickness of <15 km, compared to 20–26 km in central Afar and 25–40 km on the rift margins (Bastow & Keir, 2011; Hammond et al., 2011; Tiberi et al., 2005). Seismicity at ~12 km depth on the rift axis is indicative of melt storage near the base of the crust below the EAVS (Illsley-Kemp et al., 2018a) and supports the argument that extensional strain is focused on the rift axis and accommodated by magmatic intrusion (Ebinger et al., 2017; Ebinger & Casey, 2001; Hayward & Ebinger, 1996).

The EAVS is one of the most active magmatic segments in Afar. Amelung et al. (2000) identified subsidence at Gada 'Ale volcano between 1993 and 1996 attributed to magma withdrawal and normal faulting, and Nobile et al. (2012) observed an $\sim 60 \times 10^6$ m³ dike intrusion sourced from a reservoir at ~2–3 km depth below Dallol in 2004 (Figure 1a). The 2008 eruption of Alu-Dalafilla produced $\sim 25 \times 10^6$ m³ of erupted lava flows sourced from a shallow (<2 km) deep axial magma chamber (Pagli et al., 2012). Pagli et al. (2012) suggest that much of the erupted magma was present in the upper 4 km of the crust before the eruption, supporting the comparison between the EAVS and shallow sill complexes at fast-spreading MORs.

Erta 'Ale is the most persistently active volcano in the EAVS, hosting a long-lived active lava lake in the south pit of its summit caldera, with observations of lava lake activity extending for >90 years (Barnie et al., 2016; Varet, 1971) (Figure 1b). The north pit also hosted an active lava lake (Varet, 1971), which solidified between 1988 and 1992 (Field et al., 2012) but came close to reactivation in 2013 (Barnie et al., 2016). The

south pit lava lake level has fluctuated through time (Barnie et al., 2016; Le Guern et al., 1979) with overflows being observed from 1967 to 1973 (Barberi & Varet, 1970; Le Guern et al., 1979; Varet, 1971), in 2010 (Field et al., 2012), and in January 2017 (Global Volcanism Program, 2017). The only previously observed ground deformation at Erta 'Ale volcano in 2004–2005 was not associated with an overflow (Barnie et al., 2016). Barnie et al. (2016) attribute the deformation to a shallow dike intrusion aligned with the ridge axis in 2004–2005 producing 2.3×10^6 m³ of volume change. Field et al. (2012) use melt inclusions in lavas erupted in 2010 to find that the magma crystallized over a period of ~10–37 years at depths of <1.5 km, indicating the presence of a shallow reservoir below Erta 'Ale. This is in agreement with Gerlach (1980) who suggest that magma degassing originates in a large reservoir at >1 km depth.

1.2. 2017 Erta 'Ale Eruption

Erta 'Ale lava lake overflows from 16 to 19 January 2017 produced ~1 km long lava flows within the summit caldera (Global Volcanism Program, 2017). On 21 January 2017, a fissure eruption also opened ~3 km SE of the lava lake within a relic caldera on the south flank of Erta 'Ale (Figure 1b), producing the highest level of SO₂ emissions ever observed at Erta 'Ale from space (Global Volcanism Program, 2017). The lava lake level dropped at the time of the eruption by 80–100m (Volcano Discovery, 2017). Following the initial eruption, a new lava lake was formed at the eruption site, which remained active for ~1 year (Global Volcanism Program, 2018). From January 2017 until at least June 2019, the south pit lava lake and extensive lava flows originating from the eruption site have remained active, producing persistent thermal anomalies (MIROVA, 2019), and weak SO₂ emissions (Carn, 2019) detected from satellite-based sensors.

Xu et al. (2017) modeled the surface displacements from the eruption as a shallow dike intrusion fed from a vertical conduit storage below the lava lake. Their model consisted of a 3 km long dike with uniform opening below the eruption site and a volume increase of 1.9×10^6 m³; this was combined with a 1 km long dike below the lava lake with a contraction of -1.8×10^6 m³. They suggest that the dike-shaped conduit below the lava lake may be a long-lived feature of the shallow plumbing system at Erta 'Ale, with previous studies on Kilauea, Hawaii, also identifying a conduit contraction and a drop in lava lake levels during an eruption (Patrick et al., 2015, 2019a, 2019b). Xu et al. (2017) also identify an area of postintrusive uplift they model as an inflating sill below the eruption site at 1–2 km depth, indicating that the shallow axial melt observed at Alu-Dalafilla in 2008 (Pagli et al., 2012) may be representative of typical behavior on the EAVS.

Here, we use dense time series of Sentinel-1 synthetic aperture radar (SAR) observations from October 2014 to June 2019 to study ground motions associated with the January 2017 fissure eruption, as well as long-term trends of deformation at Erta 'Ale in the period building up to and following the initial eruption. We also assess how shallow magma storage is accommodated at Erta 'Ale using pressure change calculated from changes in the height of the Erta 'Ale lava lake and the volume of material extruded from the eruption site. We propose a simple mechanical model to describe the behavior of the shallow plumbing system at Erta 'Ale volcano and discuss the implications for the dynamics of magmatic centers in rift zones.

2. InSAR Data

We use all the acquisitions of Sentinel-1A/B satellites from ascending track 14 (T14A) and descending track 79 (T79D) between October 2014 and June 2019 to measure surface deformation. We create a network of 204 ascending and 300 descending interferograms using GAMMA (Werner et al., 2000) and LiCSAR software (González et al., 2016) at 5:1 range to azimuth looks, equating to ~20 × 20 m pixel size. We correct for topography using the 30 m Shuttle Radar Topography Mission elevation model (Farr & Kobrick, 2000). We perform postprocessing on the network of interferograms, to correct for a linear relationship between height and phase due to the atmosphere in each interferogram using a ~14 × 7 km nondeforming region ~15 km to the south of Erta 'Ale volcano with similar topography (Elliott et al., 2008). We calculate the performance of this correction from the mean variance of the whole background nondeforming region by masking out the ~15 × 12 km deforming area, centered on the eruption site, for all images. This results in a mean reduction in the phase root-mean-square error (RMSE) in individual interferograms of ~9% (~1 mm). We find that this linear height-phase atmospheric correction performs better on this small region around Erta 'Ale than a correction based on the GACOS atmospheric model (Yu et al., 2017, 2018), in which the mean RMSE is increased by ~90%. We reference each interferogram to its background mean value.

To estimate the time-varying atmospheric noise in the time series, we estimate the contribution of the atmospheric phase screen (APS) to each epoch in the same background nondeforming region. To do this, we

apply a least-squares inversion to find the time series of deformation in the nondeforming region using a small-baseline methodology (e.g., Berardino et al., 2002; Lanari et al., 2004, 2007). We include a minimum of three interferograms covering each deformation step. We then estimate the remaining APS from the time series within the subset by first high-pass filtering in time by applying and then subtracting a low-pass weighted Laplacian filter from the time series. We then low-pass filter in space using a $\sim 100 \times 100$ m Gaussian kernel to give an estimate of the APS for each epoch. To estimate the level of noise for each epoch, we calculate the variance of phase by differencing the filtered (APS removed) and the unfiltered time series, assuming that within this subset region, all phase variations in the filtered time series are due to noise and not ground deformation. A small amount of residual noise remains associated with each epoch, resulting from small unwrapping and filtering errors, and random noise. We account for this by calculating the sum around a loop of interferograms associated with the epoch and find that the mean residual phase is ~ 5 mm. We apply this noise value to each date in addition to the atmospheric noise calculated previously.

We perform a small-baseline style least-squares inversion for the line of sight (LOS) displacement time series across the whole image for all time steps, incorporating the calculated variance on each epoch as weights using a variance-covariance matrix. This approach allows us to propagate the calculated data noise estimates into errors in displacement for each epoch, accounting for the variability in noise between epochs. We perform no further filtering on the whole image time series. Further details are provided in the supporting information.

With ascending and descending data, we only have two components of a 3-D displacement field (e.g., Wright et al., 2004). We use the ascending and descending data to invert for rift-perpendicular horizontal and vertical ground movement at Erta 'Ale, assuming all horizontal displacements are perpendicular to the ridge axis (e.g., Hamling et al., 2014). We solve for rift-perpendicular horizontal and vertical motions only where ascending and descending acquisition dates align to within $\lesssim 1$ week in order to limit the amount of deformation that occurs between acquisitions.

3. Analysis

3.1. Ground Deformation

Figure 2 shows the full time series of surface displacements from October 2014 to June 2019 for ascending LOS, descending LOS, horizontal rift-perpendicular, and vertical motions. We divide the time series into four stages: the preeruption period from October 2014 to January 2017 (A), the initial intrusion in January 2017 (B), the early-stage eruption from January 2017 to April 2017 (C), and the late-stage eruption from April 2017 to June 2019 (D). Due to the lack of ascending acquisitions between February 2017 and September 2017, we combine Periods C and D into a single late-stage eruption period from January 2017 to June 2019 (E) so that we can resolve horizontal rift-perpendicular and vertical motions. We extract the time series for six representative points around Erta 'Ale volcano (numbered 1–6 in the upper left panel of Figure 2), which are displayed in Figure 3. We selected the points in order to observe displacements as close as possible to the lava lake (1 and 2) and eruption site (4–6) while avoiding incoherence in the time series associated with lava flows and rapid cointrusive surface displacements. Below, we describe how Erta 'Ale deformed in each of the key time periods and discuss best fit simple models that can explain the observations.

3.1.1. Preeruption (A)

Time Period A in Figures 2–4 shows surface displacements in the buildup to the eruption between October 2014 and January 2017. This period is dominated by a gradual increase in rift-perpendicular extension focused on the rift axis between the lava lake and eventual eruption site (Figure 2). The total extension over the rift axis is shown in Figure 4 and reaches a maximum of 140 ± 10 mm before the eruption date in January 2017 at an average rate of 60 ± 10 mm/year, more than 3 times higher than the average plate spreading rate at Erta 'Ale. The extension rate also increases around April 2016 from a rate of 35 ± 7 to 111 ± 30 mm/year up to the eruption date. Vertical displacements during this period are small at ± 4 – 10 mm/year, with slight uplift observed on the rift axis between the lava lake and eruption site.

We model the total observed extensional signal (October 2014 to January 2017) with the opening of a vertical dike structure aligned with the rift axis and assuming deformation is caused by dislocations in an elastic homogeneous half-space (Okada, 1985). To find this solution, we subsampled the data using a quadtree approach (Jónsson et al., 2002), with a variance threshold of 9×10^{-4} m². We optimized the geometry and opening of the dislocation and estimated uncertainties using the Geodetic Bayesian Inversion Software,

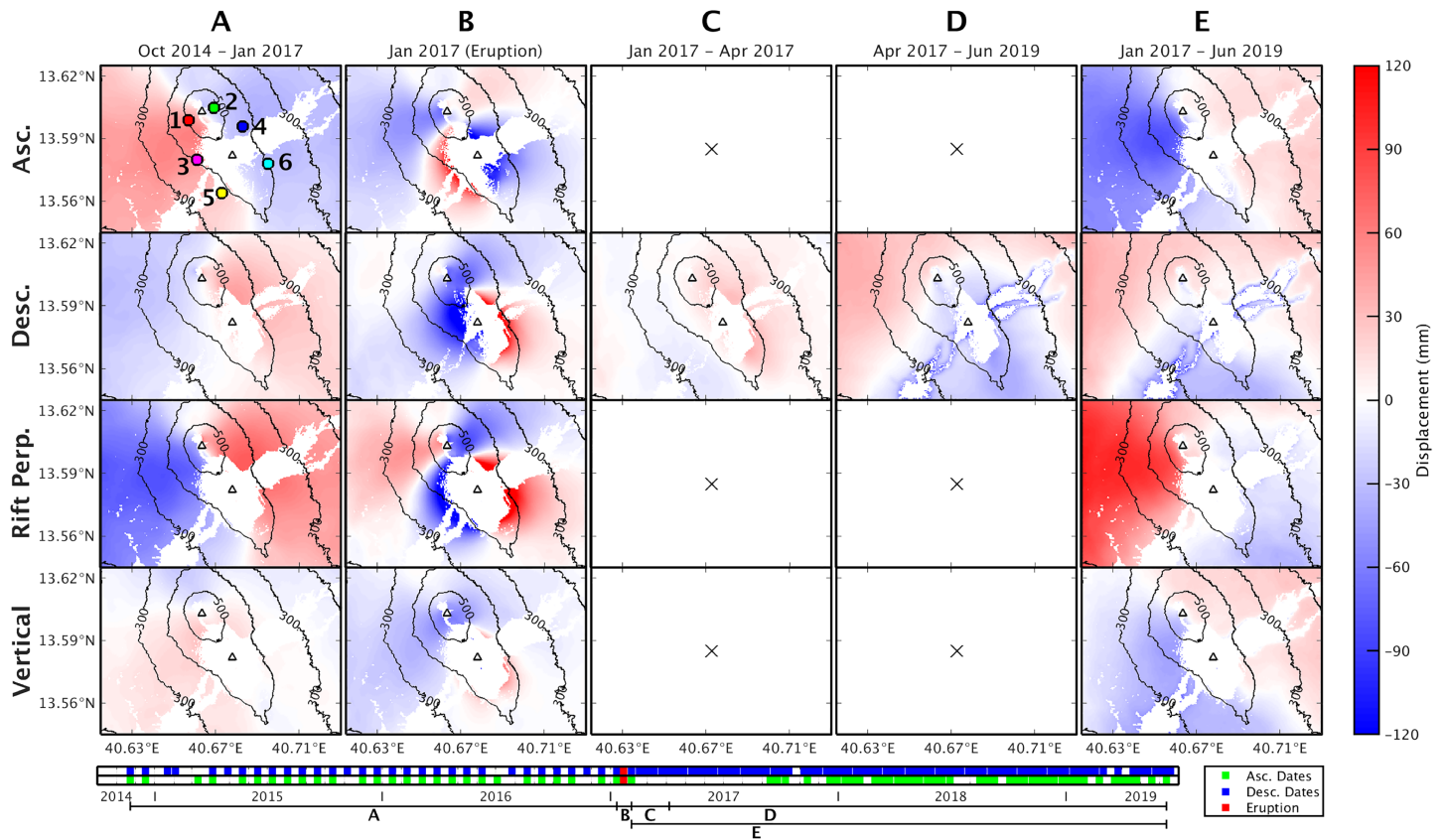


Figure 2. Displacement maps at Erta 'Ale volcano in the buildup to (A), during the initial stage (B), and during later stages (C–E) of the eruption, for ascending LOS, descending LOS, horizontal rift-perpendicular, and vertical motions (as in Figure 3). As ascending data are missing during Periods C and D, we are unable to resolve rift-perpendicular and vertical motions for these periods. For the ascending and descending LOS maps, positive values show motion toward the satellite; for the rift-perpendicular maps, positive values show motion to ~NE; and for the vertical maps, positive values show uplift. Topographic contours are shown on every map for reference at 100 m spacing, along with the Erta 'Ale lava lake and south flank eruption site (triangles). The six colored points around Erta 'Ale are the points selected to show the time series of displacements in Figure 3. The points were selected in order to be as close to the lava lake and eruption site as possible, without losing coherence (white mask on maps). The preintrusive and cointrusive phases (A–E) are shown on the time axis, with the acquisition dates for ascending and descending Sentinel-1A/B, and the eruption date.

which implements the Markov Chain Monte Carlo method and Metropolis-Hastings algorithm to create probability density functions of model source parameters (Bagnardi & Hooper, 2018).

The best fit vertical dike has dimensions $\sim 5 \times 5$ km with depth to the top of the dike at ~ 500 m; it is aligned with the rift axis and has a volume increase of $\sim 3 \times 10^6$ m³ (a full list of model parameters and uncertainties is shown in Table 1). Ascending and descending data, model, and residual interferograms are shown in Figure S2. This model has a similar geometry to both a preeruptive dike between January 2016 and January 2017 modeled by Xu et al. (2017) and a dike observed in 2004–2005 by Barnie et al. (2016) at Erta 'Ale, which did not lead to an eruption. The similarity between the modeled dikes in 2004–2005 and 2014–2017 suggests that this style of intrusion may be typical at Erta 'Ale and could be indicative of a long-lived region of accumulating shallow melt which is elongated along the ridge axis.

3.1.2. Initial Eruption (B)

Ground observations show that the eruption began on 21 January 2017 (Global Volcanism Program, 2017) on the south flank of Erta 'Ale. The first posteruption image was acquired on 28 January 2017. From 11 to 28 January 2017, we measure up to 400 ± 50 mm of extension over the ridge and 50 ± 10 mm of uplift at the eruption site (Points 1 and 2 in Figures 2–4). At the same time, we measured up to 120 ± 20 mm of contraction and 60 ± 10 mm of subsidence near the lava lake (Points 3–6 in Figures 2–4).

We can model this deformation well using two vertical dike sources, one opening below the eruption site and one closing below the summit caldera. We tried a variety of simple source mechanisms for the closing about the summit caldera signal including point and spherical sources, although a contracting planar dike

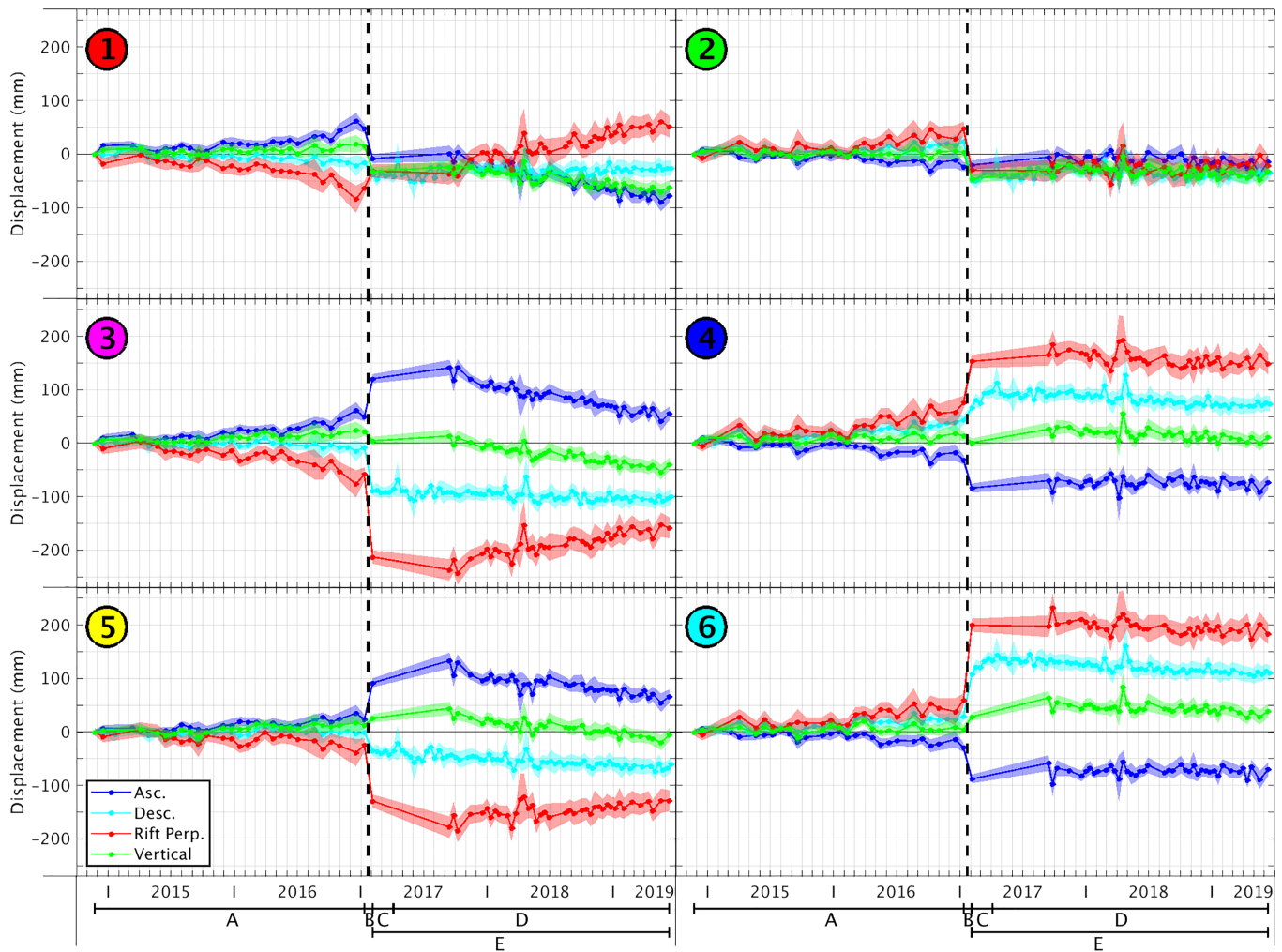


Figure 3. Time series of ascending LOS (dark blue), descending LOS (light blue), rift-perpendicular (red), and vertical (green) displacements at six points around Erta 'Ale volcano as shown in Figure 2. Points 1 and 2 are about the lava lake, Points 3 and 4 are to the north of the eruption site, and Points 5 and 6 are to the south of the eruption site. Points 1, 3, and 5 are on the SW side of the ridge, and Points 2, 4, and 6 are on the NE side of the ridge. The points were selected in order to be as close to the lava lake and eruption site as possible, without losing coherence. Time periods shown in Figure 2 are shown below the time axis for preeruption (A), during the initial eruption (B), and during later stages of the eruption (C–E).

provided a significantly better fit than sources with radially symmetric deformation patterns. Below the summit caldera, we require a larger value of dike closing at depths ≥ 900 m than at depths ≤ 900 m (Figure 5), as a single value of closing is not able to fully reproduce the deformation pattern. For the portion of the data that shows contraction about the summit caldera, a single value of dike closing is not able to match the magnitude of far-field displacements (>2 km from the summit caldera) without producing excessive near-field displacements (<1 km from the summit caldera). We preferred to keep the model relatively simple, with two sources, rather than solving for a full distributed contraction model.

Parameters for the modeled dikes with error estimates are shown in Table 1 with volume changes for the Dikes 2 (contraction under the lava lake) and 3 (extension SE of the lava lake) of $-1.9 \pm 0.3 \times 10^6$ and $1.59 \pm 0.04 \times 10^6$ m³, respectively. Predicted displacements from the model are represented in Figures 5b and 5e for ascending and descending LOS geometry and shown in depth cross section in Figure 5g. Areas of incoherence near the eruption site in Figures 5a–5f are due to either fresh lava flows or the high deformation gradient associated with the intrusion.

Our findings for the geometry of the shallow dikes agree well with that found by Xu et al. (2017), who also suggest there were two subvertical dikes, opening below the eruption site and a contracting dike below the Erta 'Ale lava lake. Our model reduces the RMSE of ascending and descending data by 45% in the area shown

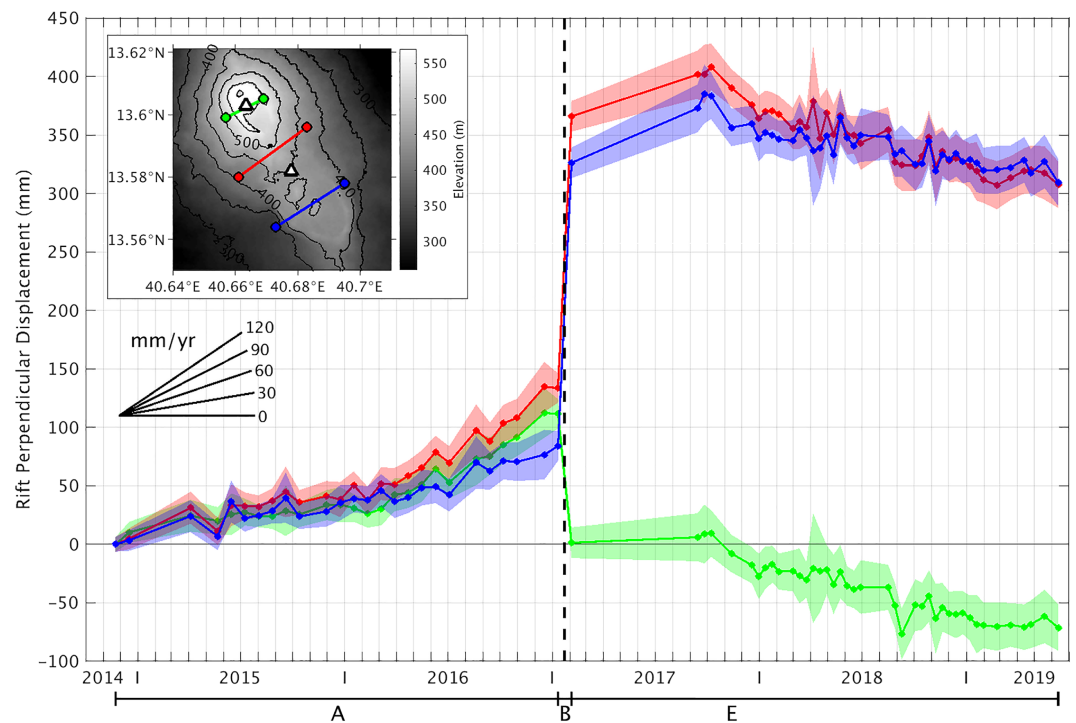


Figure 4. Time series of horizontal rift-perpendicular displacements between three pairs of points over the ridge axis at Erta 'Ale. Inset map shows the location of the pairs of points used. The points used are the same as shown in Figures 2 and 3 and are selected to be as close to the lava lake and eruption site as possible, without losing coherence. Green = Points 1 and 2; Red = Points 3 and 4; Blue = Points 5 and 6. The eruption date in January 2017 is marked by a black dashed line. The preintrusive and cointrusive phases shown in Figure 2 are indicated below the time axis.

in Figures 5a–5f, compared to a reduction of 32% for the model of Xu et al. (2017). Some residuals remain close to the eruption site, which are likely due to simplifications we have made in the model, such as the uniform opening of rectangular planar dikes and the use of an elastic homogeneous half-space. Because of these simplifications, the model cannot fully reproduce the complex cointrusive deformation pattern produced in the near-field. Additional residuals, particularly away from the eruption site, may be mostly due to uncorrected atmospheric errors.

We interpret the dike below the lava lake as a contracting tabular conduit, reaching down to 900–950 m depth. Below this, there is an increase in dike contraction below the lava lake, coincident with the depth of the bottom of the intruding Dike 3. Here, we cannot resolve in more detail the structure of this region of higher contraction, but considering the presence of melt storage at ~ 1 km depth elsewhere on the EAVS (Pagli et al., 2012) and the inference of shallow melt storage below Erta 'Ale (Field et al., 2012), it may represent the top of a region of shallow storage at Erta 'Ale volcano at ~ 1 km depth.

3.1.3. Late-Stage Eruption (C–E)

After the initial intrusion in January 2017, the eruption site on the south flank of Erta 'Ale remained active and produced extensive lava flows, which are still active at the time of writing (August 2019), ~ 2.5 years later. In the descending time series, regular 12-day acquisitions from February to September 2017 allow us to separately explore LOS motions between January and April 2017 (C) and April 2017 and June 2019 (D). During Period C, a gradual range decrease (apparent uplift) signal of 45 ± 15 mm can be seen in the descending time series in Figures 2 and 3, at Points 4 and 6 on the east side of the rift axis. Xu et al. (2017) model this apparent uplift signal as a shallow sill inflation at ~ 1 – 2 km depth, similar to sills observed elsewhere on the EAVS during eruptions (e.g., Pagli et al., 2012). From April 2017, this gradual uplift is followed by a period of slow range increase (gradual apparent subsidence) of roughly equal magnitude to the uplift between January and April 2017, resulting in small total displacements for Time Period E (C + D).

After the initial response to the eruption between January and April 2017 (C), the long-term response up to July 2019 (D) shows gradual rift-perpendicular contraction and subsidence at rates of 50 ± 20 and

Table 1
Table of Dike Model Parameters (All to Three s.f.) for Preeruptive (1) and Cointrusive Dikes (2a, 2b, and 3; see Figure 5)

		Depth (m)	Length (m)	Height (m)	Opening (m)	Volume ($\times 10^6 \text{m}^3$)
Dike 1	2.5%	463	3,420	3,940	0.108	1.46
	Optimal	528	5,250	4,940	0.130	3.37
	97.5%	861	7,400	4,990	0.205	7.57
Dike 2a	2.5%	—	898	891	−0.134	−0.104
	Optimal	0.01*	902	922	−0.133	−0.111
	97.5%	—	915	955	−0.130	0.117
Dike 2b	2.5%	891	898	2,080	−0.931	−1.57
	Optimal	922	902	2,250	−0.886	−1.80
	97.5%	955	915	2,470	−0.841	−2.10
Dike 3	2.5%	—	3,270	626	0.759	1.55
	Optimal	0.01*	3,280	635	0.763	1.59
	97.5%	—	3,280	640	0.771	1.62

Note. The 2.5 and 97.5 percentiles of the probability distribution functions for each parameter are shown alongside the optimal model. Parameters marked with * are fixed. We fix the dip of all dikes to 90°. Depth is to the top of the dikes. Bold rows are used to emphasize the optimal solutions, rather than the 2.5% and 97.5% error bounds.

25 ± 15 mm/year, respectively (Figures 3 and 4). The horizontal contraction is focused near the rift axis between the lava lake and eruption site, while the vertical subsidence is asymmetric over the rift axis and focused on the SE side of the edifice. We find that no simple source is able to fully reproduce the ascending and descending data from September 2017 to July 2019 (D). A vertically orientated prolate spheroidal source (Yang et al., 1988) produces the closest match, but the combination of a broad vertical signal and a sharp transition in the horizontal signal over the rift axis suggests there might be a vertically extended source. Using a Yang source, we find that it must be in an off-rift position, ~3 km to the SW of the eruption site, with a depth extent of ~1–14 km, and a volume change of ~20–70 × 10⁶ m³ (Figure S3).

3.2. Lava Lake Level and Pressure Changes

3.2.1. Lava Lake Depth From SAR

Changes in lava lake levels are potentially a direct measure of changes in pressure in a shallow magma chamber and have been used extensively to assist the understanding of shallow plumbing system dynamics at Kilauea (Patrick et al., 2015; Poland & Carbone, 2018), Villarrica (Moussallam et al., 2016), Erebus (Jones et al., 2015; Oppenheimer et al., 2009), Nyiragongo (Burgi et al., 2014), and Erta 'Ale (Barnie et al., 2016; Field et al., 2012). Here, we use full resolution Sentinel-1 SAR intensity images (~5 × 20 m pixel spacing) to estimate the depth of both the south (active lava lake) and north pits at Erta 'Ale from the observed shadow lengths (see Figure 6). We define regions in shadow by a simple threshold in the reflection intensity and count the length of shadows in range by the number of pixels that fall below the threshold. We show an example in Figure S4. The method works well when the shadow is well defined, but for some acquisitions, the shadow limits are more uncertain. For example, the north pit shadow in Figure S4a is not well defined on the far range side. For this calculated shadow length of 7 pixels (~8 m pit depth), we give confidence bounds that the shadow is 6–14 pixels long (~15–42 m pit depth). In contrast, the south pit shadow in Figure S4b has sharp edges, and we can give narrow confidence bounds in the shadow length of ±1 pixel (±3 m pit depth). Pit depths of 0 m refer to when the pits are full (level with the pit rim) or overflowing.

Figures 7 and S5 show the time series of pit depths for the south and north pits, respectively, at Erta 'Ale, from October 2014 to June 2019, from both ascending and descending Sentinel-1 intensity shadows. As shown in Figure S5, we validate these measurements using field reports (Volcano Discovery, 2017), where the lava lake depth in the south pit is routinely reported, and lava lake depth estimates from tourist photos taken of the lava lake from the web (see Table S1 for citations). We estimate uncertainties in field reports and tourist photos from either accompanying reports or, in the case of some tourist photos, estimations of depth using local features for scale. In general, these supporting information agree well with depths calculated from

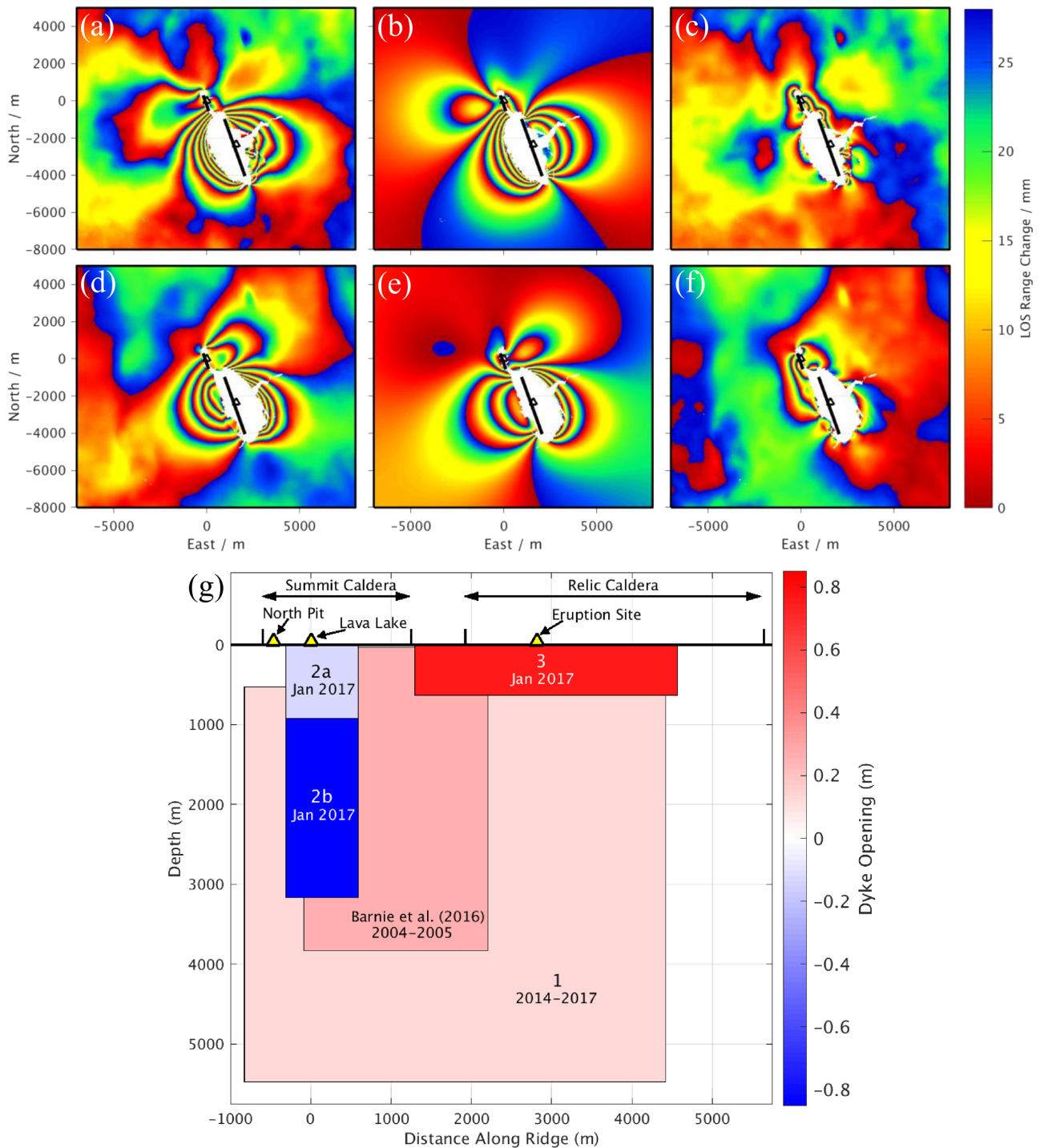


Figure 5. (a–c) Ascending and (d–f) descending Sentinel-1 data, model, and residual for cointrusive interferograms 11 January 2017 to 4 February 2017 and 4 January 2017 to 28 January 2017, respectively. One color cycle (red–blue) represents 27 mm of line of sight range change away from the satellite. Locations of Dikes 2 and 3 are shown as black lines, with the lava lake and eruption site shown as triangles. (g) Rift-perpendicular cross-sectional view of the modeled dike structure, where Dike 1 is preeruptive (October 2014 to January 2017), and Dikes 2a, 2b, and 3 are cointrusive. Dike geometries were optimized using GBIS (Bagnardi & Hooper, 2018), with the parameters shown in Table 1. Also shown is the modeled dike from Barnie et al. (2016) from January 2004 to May 2005. Locations of the lava lake, north pit, and the eruption site are shown as yellow triangles, with the locations of the summit and relic calderas also shown.

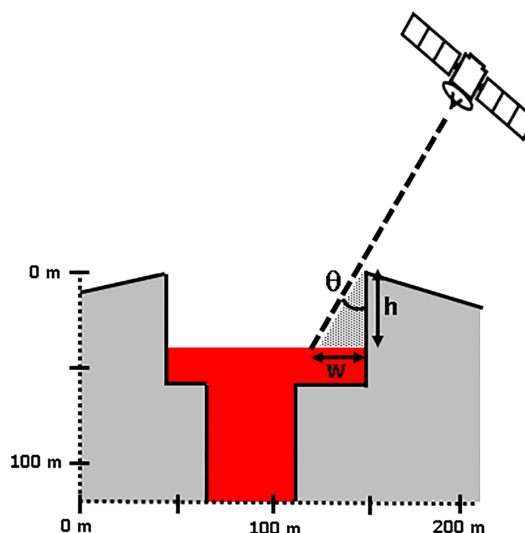


Figure 6. Sketch showing how we use SAR shadow lengths (w) and look angle (θ) to calculate pit depth (h). A lava lake depth of 0 m is when the lake level reaches the pit rim.

Sentinel-1 intensity shadows for the south pit. We cannot apply the same check to the north pit (Figure S6) as it is not routinely visited by tourists or field guides.

In the preeruption period (A), both the north and south pit levels were stable at shallow depths of <20 and $\lesssim 40$ m for the south and north pits, respectively (Figures 7 and S4), with lava lake overflows reported in January 2016, November 2016, and January 2017 (Volcano Discovery, 2017). As we only use Sentinel-1 for this study, we cannot measure surface displacements or lava lake levels earlier than October 2014. Barnie et al. (2016) monitor the Erta 'Ale lava lake levels from 2000 to 2015 using optical satellite imagery. From 2011 to 2015, following a period of lava lake overflows in 2010 (Field et al., 2012), the lava lake was at 20 ± 10 m depth (Barnie et al., 2016), suggesting that the high lava lake levels we observe in Period A extend back to the last significant lava lake overflow in 2010. Over the eruption date (black dashed line), the lava lake level in both pits dropped rapidly to 80–100 and 100–140 m in the south and north pits, respectively. This is coincident with reports of a small plume arising from the south pit of Erta 'Ale at this time due to partial pit rim collapse (Global Volcanism Program, 2017) and the opening of the new eruption site and lava flow emplacement on the south flank of Erta 'Ale.

From January 2017 to June 2019, the north pit level has remained roughly stable at depths of 80–130 m. Between January and April 2017 (Time Period C), the south pit lava lake rose from 90 ± 10 to 60 ± 10 m depth, at the same time as the sill inflation at 1–2 km depth, modeled from surface uplift in Time Period C by Xu et al. (2017). Between April 2017 and June 2019 (Time Period D), the lava lake level dropped gradually from 50 to 70 m back to the levels just after the eruption date of 80–100 m. As shown in Figure 7, this variation in lava lake level is temporally correlated with the descending LOS surface displacement time series with an apparent inflation and deflation of 45 ± 15 mm. This correlation supports the hypothesis that the south pit lava lake may be a good indicator of the pressure state in the shallow plumbing system at Erta 'Ale, similar to the Halema'uma'u lava lake at Kilauea, Hawaii (Patrick et al., 2015, 2019b). The north pit may not be as responsive to pressure changes due to the surface being solidified since ~ 1990 (Field et al., 2012).

3.2.2. Lava Lake Pressure and Deformation

We use simple analysis of changes in pressure to investigate the state of the Erta 'Ale shallow plumbing system during the eruption period, following the approach previously used for the lava lake at Kilauea (e.g., Poland & Carbone, 2018). If the magma is homogeneous and incompressible, the change in pressure required to sustain pit levels in hydrostatic equilibrium (ΔP) from the observed changes in pit heights (Δh) is $\Delta P = \rho g \Delta h$, where g is the acceleration due to gravity (9.8 m/s^2). For magma density, ρ , we use a value of $2,550\text{--}3,100 \text{ kg/m}^3$ (Anderson & Poland, 2016), using Kilauea volcano, Hawaii, as a close analog of the Erta 'Ale system. We use a large range in density as the gas content in the magma at Erta 'Ale is unknown. We find that for a cointrusive drop in lava lake levels of 90 ± 10 m, the associated pressure loss is 2.5 ± 0.5 MPa,

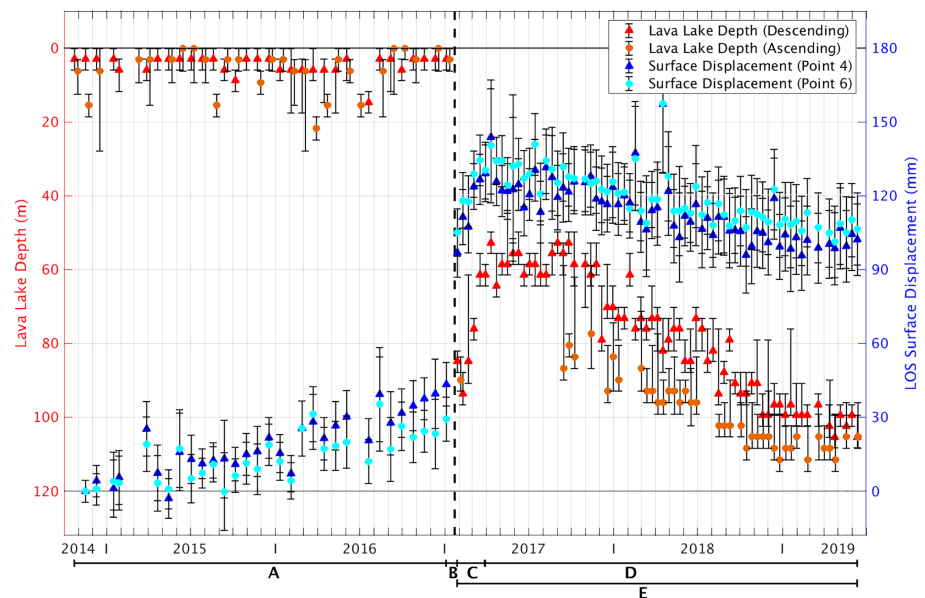


Figure 7. (left axis, red) Time series from October 2014 to June 2019 of Erta 'Ale lava lake depths calculated from Sentinel-1 ascending (orange circles) and descending (red triangles) SAR shadows. (right axis, blue) Descending Sentinel-1 line of sight surface displacement time series at Points 4 (dark blue triangles) and 6 (light blue circles) (see Figures 2 and 3). Points 4 and 6 were selected as they lie closest to the maximum of the area of postintrusion inflation in Time Period C (Figure 2). The eruption date in January 2017 is marked by the black dashed line. A lava lake depth of 0 m represents when the lake is level with the pit rim (Figure 6). Time Periods A–E, as shown in Figure 2, are indicated below the time axis.

and for the postintrusive rise and fall of the lava lake of 30 ± 20 m, the magnitude of pressure change is 0.8 ± 0.6 MPa.

Using the pressure changes calculated from lava lake level rise and fall, we use a boundary element model to establish whether the changes in pressure observed at the lava lake can reproduce the surface deformation observed at Erta 'Ale. We use the same cointrusive dike geometry modeled previously (Figure 5), divided into $\sim 150 \times 150$ m patches, within a homogeneous elastic half-space. Using the cointrusive pressure change, we solve for the magnitude of patch opening and then convert into surface displacements using Okada's formulation (Okada, 1985). The magnitude of patch opening required to produce surface displacements is also dependant on the elastic shear modulus of the medium.

We find that for a pressure change of 2.5 ± 0.5 MPa, we can match the magnitude of the cointrusive deformation signal shown in Figure 5, if the shear modulus is 6 ± 2 GPa. Within error, this value is consistent with the range of 7.5–13 GPa calculated by Hammond et al. (2011) for the upper 3 km of the Afar crust. It has also been previously established that the shear modulus close to the summit of basaltic shield volcanoes can be significantly lower than estimates from seismic studies (Hooper et al., 2002). At Kilauea, Hawaii, Hooper et al. (2002) estimated the shear modulus in the upper 2.7 km to be 4.5 GPa, while Montagna and Gonnermann (2013) use a shear modulus of 3 GPa, for modeling flow through a horizontal dike between the Kilauea summit and Pu'u'O'o. As our model is consistent with these previous findings, we suggest that a shear modulus of 4–8 GPa is applicable to Erta 'Ale, and the lava lake level is sensitive to the pressure changes in the shallow plumbing system associated with the January 2017 intrusion.

3.3. Lava Flow Extent and Effusion Rate

We monitor the growth of extensive erupted lava flows by tracking changes in descending Sentinel-1 coherence. We use only the descending track due to the gap in ascending data between February and September 2017. The coherence of a pixel is an estimate from the similarity of phase scatterers from a group of neighboring pixels in an interferogram (e.g., Massonnet & Feigl, 1998). Areas where the ground does not change between passes, such as the arid environment around Erta 'Ale, produce very high coherence; changing surfaces, such as vegetation, water, or active lava flows, result in low coherence (Massonnet & Feigl, 1998; Rosen et al., 1996). We use this contrast between the background level of high coherence and the low coherence

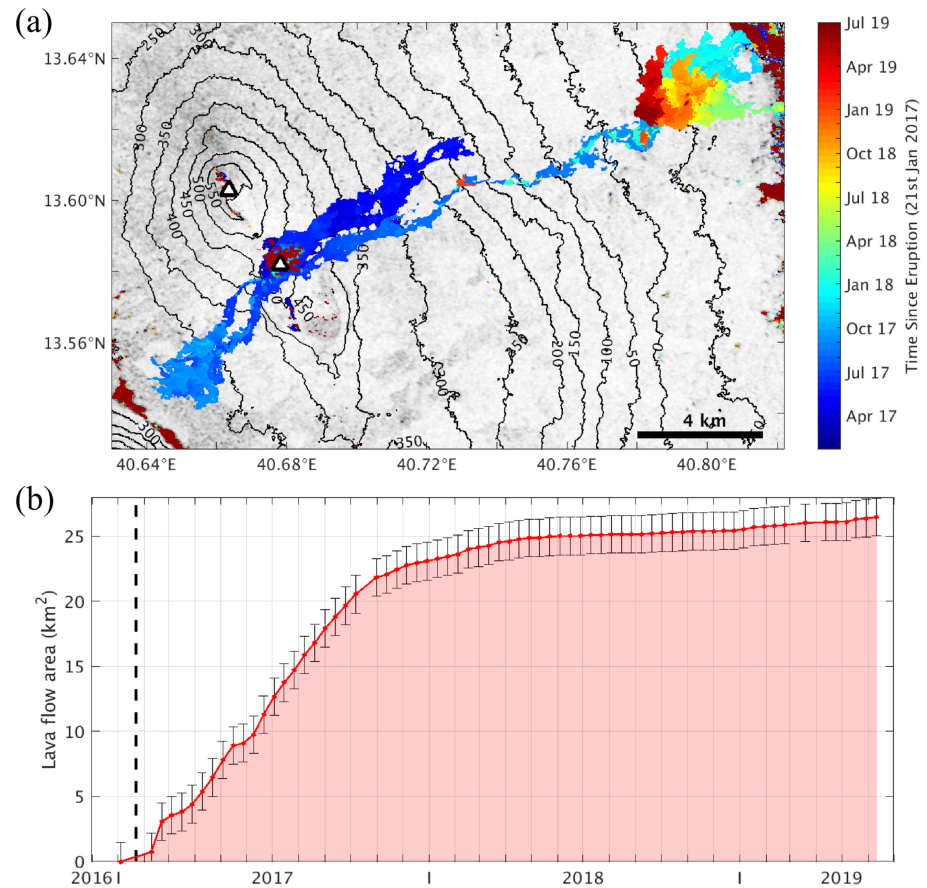


Figure 8. (a) Lava flow coverage from the eruption site and lava lakes (white triangles) at Erta 'Ale from the eruption date (21 January 2017) to June 2019. We define fresh lava flows as all incoherent pixels (coherence < 0.35) as typically the background coherence at Erta 'Ale is very good. Background image shows the coherence of a preeruption 24-day interferogram on a 0-1 gray scale. Areas of additional incoherence in the NE and SW of the image are likely due to small patches of vegetation. The 50 m contours show the topography around Erta 'Ale volcano. (b) Cumulative lava flow area from the eruption date (black dashed line) to March 2018. We calculate error bounds based on the mean preeruption incoherence of the area (incoherence not associated with lava flows).

of fresh lava flows to identify regions of active lava flow at Erta 'Ale, following the approach used to monitor lava flow growth in other locations such as Hawaii (Dietterich et al., 2012). We identify pixels with low coherence using a threshold value of 0.35. We calculate the area covered by lava flows by summing the area extent of incoherent pixels identified for each postintrusive interferogram. Areas of speckly noise in the NE and SW corners of Figure 8a are likely due to small areas of vegetation. To account for this noise, we use all 29 preeruption 24-day interferograms (there are no 12-day preeruption interferograms available) of the same region shown in Figure 8a to establish a mean value for the amount of noise the small areas of vegetation produce. We then use this noise value to give error bounds on the lava flow area calculated in this region.

From January 2017 to June 2017, flows extended <7 km to the NE of the eruption site, before developing new flows to the SW (<6 km long). Between July and October 2017, a thin, rapidly extending flow occurred to the NE (<14 km long). From October 2017 to at least June 2019, lava flows have remained active (MIROVA, 2019) and pooled in a basin region 14–16 km to the NE of the eruption site where the topographic gradient is shallow. Figure 8b shows a roughly linear flow area growth rate from the eruption up to November 2017, where the total flow area begins to level off at ~22 km². As there are no intensity shadows originating from the lava flows, the thickness of the flow is ≤15 m. Using the anecdotal evidence from a local field guide during a short field campaign in September 2017, we estimate the thickness of lava flows around this time to be in the range 0.5–2.5 m. This is in agreement with tourist photographs of the fresh lava flows which show thicknesses of 0.5–1 m at the SW extent of the flows (Global Volcanism Program, 2018). Applying this to a total area of lava flow coverage of 26 ± 1 km², we estimate the total volume of erupted material up to

June 2019 is in the range $12.5\text{--}67.5 \times 10^6 \text{ m}^3$. This is in agreement with our estimate of $20\text{--}70 \times 10^6 \text{ m}^3$ from the deflation of an off-rift vertically extensive source during the long-lived eruption (September 2017 to July 2019).

We measure the effusion rate over the period of approximately linear growth in lava flow area shown in Figure 8b up to October 2017. Between November 2017 and October 2018, the flow area does not significantly increase. Persistent thermal anomalies from satellite-based MODIS data show that the NW extent of the flow has remained active up to at least June 2019 (MIROVA, 2019), indicating that the flow in this area may be thickening. Field reports are unable to validate this as the area is highly inaccessible. However, for the period of linear flow area growth, we can measure the effusion rate from the eruption date (21 January 2017) to 7 October 2017 (271 days). We find that for a total erupted area of $21 \pm 2 \text{ km}^2$, the erupted volume is $10\text{--}58 \times 10^6 \text{ m}^3$, with a mean effusion rate of $0.4\text{--}2.5 \text{ m}^3/\text{s}$. This rate is in agreement with the 2010 lava lake overflows where Field et al. (2012) estimate that the gas flux could be accounted for by a near-complete degassing of magma in the conduit, moving at rates of $1.1\text{--}2.6 \text{ m}^3/\text{s}$.

4. Discussion

Several key features of the Erta 'Ale shallow plumbing system show similarities to other volcanoes such as Kilauea and Mauna Loa, Hawaii, and Ambrym, Vanuatu, with the removal of melt from a summit caldera coincident with the horizontal propagation of a dike into an established rift zone (e.g., Amelung et al., 2007; Montagna & Gonnermann, 2013; Poland et al., 2014; Shreve et al., 2019). At Kilauea, a synthesis of measurements, including InSAR, GPS, tilt, and gravity, reveal a shallow magma reservoir at $\sim 1.5 \text{ km}$ depth below the Halema'uma'u lava lake (Anderson et al., 2015; Bagnardi et al., 2014; Poland et al., 2014). At Erta 'Ale, pressure changes in the lava lake during the postintrusion period are linked to the shallow sill inflation and subsequent deflation at $1\text{--}2 \text{ km}$ depth (Xu et al., 2017). Our cointrusive model also requires an increase in dike contraction at $\sim 1 \text{ km}$ depth, indicating a change in subsurface conditions. The presence of a shallow sill overlying a dike structure at Erta 'Ale is in agreement with analysis by Xu et al. (2017) of the stress state below Erta 'Ale from topographic loading. Axis-aligned dike structures are preferred to sills within $\sim 5 \text{ km}$ either side of the ridge axis and up to $\sim 10 \text{ km}$ depth, except directly below the summit caldera where the relative topographic unloading allows the formation of sill structures within $\sim 0.5 \text{ km}$ either side of the ridge axis and up to $\sim 1\text{--}1.5 \text{ km}$ depth (Xu et al., 2017). Combined with petrological evidence of a potential reservoir at $<1.5 \text{ km}$ depth (Field et al., 2012), we propose that a shallow reservoir on the ridge axis is present at Erta 'Ale at $\sim 1 \text{ km}$ depth, which likely sustains the long-lived lava lake.

A common feature of shallow plumbing systems in rift zones is the connectivity a shallow reservoir to a deeper magma chamber. At Kilauea, a reservoir at $3\text{--}5 \text{ km}$ depth is connected to both the shallow reservoir at Halema'uma'u and the East Rift Zone (Poland et al., 2014). On the EAVS, a magma reservoir at 4 km depth at Alu-Dalafilla was observed during the 2008 eruption and shallow sill inflation (Pagli et al., 2012). From subsidence and contraction during the long-lived eruption (2017–2019), we infer a vertically extensive source from depths of $\sim 1\text{--}14 \text{ km}$, which is more likely representative of a system of smaller stacked sources, than a single body. The large preruptive axial dike inflation, which is similar to a previous intrusion at Erta 'Ale (Barnie et al., 2016), may also indicate that shallow melt at Erta 'Ale is not stored in a relatively contained magma reservoir but is distributed through a zone of partial melt in the upper $\sim 5 \text{ km}$ of the crust. A heavily intruded shallow crust may be typical on the EAVS, as most of the erupted material from the 2008 Alu-Dalafilla eruption was sourced from within the upper 4 km of the crust (Pagli et al., 2012). Illsley-Kemp et al. (2018a) also identify a lower crustal reservoir below Alu-Dalafilla from seismicity at $\sim 10\text{--}15 \text{ km}$ depth and suggest that a similar feature below Erta 'Ale may be present but was not detected in their study due to a potentially high melt percentage in the crust. This is in agreement with the presence of a system of stacked midcrustal sources from our analysis of surface deformation from 2017 to 2019 and with receiver function studies which identified a significant amount of magmatic intrusion in the Afar lower crust (e.g., Hammond et al., 2011).

During the preruption period, gradual dike opening along the rift axis corresponds to a total volume increase of $1.5\text{--}7.6 \times 10^6 \text{ m}^3$, at a rate of $0.02\text{--}0.11 \text{ m}^3/\text{s}$. As the lava lake level does not significantly vary throughout this period, the pressure state in the shallow reservoir is stable. In order to maintain a steady pressure state at the top of the preruptive dike, magma flux from depth must be compensating for the extension on the rift axis at a rate at least equal to the opening of the dike. We can therefore give a lower bound

estimate on magma flux during this period of $0.02\text{--}0.11\text{ m}^3/\text{s}$. The lack of any significant ground deformation across the total postintrusive period indicates that the majority of erupted material is either being sourced from depth or is highly compressible (Rivalta & Segall, 2008). The eruption rate of $0.4\text{--}2.5\text{ m}^3/\text{s}$ may therefore be a good indicator of magma flux through the shallow plumbing system during Period E, up to 2 orders of magnitude larger than our estimate of magma flux during Period A. The large volume of erupted material, in comparison to the volume of observed shallow intrusions at Erta 'Ale, is supported by Hutchison et al. (2018) who use petrology to establish that two thirds of material at Erta 'Ale is erupted and one third intruded into the shallow crust. This is in agreement with seismic evidence which suggests that during the final stage of breakup on the EAVS, there is a shift from intrusive to extrusive magmatism (Keir et al., 2013).

The presence of a potential shallow reservoir overlying a region of axial melt storage at Erta 'Ale and Alu-Dalafilla on the EAVS (Pagli et al., 2012) shows similarities to the stacked sill structure observed at spreading ridges with high melt flux, such as the fast-spreading EPR (e.g., Carbotte et al., 2013; Marjanović et al., 2014; Wanless & Behn, 2017). An important distinction at Erta 'Ale is the largely dike-fed plumbing system, defined by the local topographic and regional tectonic stress fields (Xu et al., 2017; Wadge et al., 2016), rather than a system of stacked sills observed at MORs, although dikes at MORs may simply be difficult to image with reflection seismology (e.g., Marjanović et al., 2018). Yet the existence of a reservoir at $\sim 1\text{ km}$ depth at Erta 'Ale and Alu-Dalafilla indicates that shallow magma bodies may be supported on the EAVS. High melt flux on the EAVS may be contributing to this, given the heavily intruded crust beneath the Danakil Depression (Bastow & Keir, 2011; Hammond et al., 2011; Tiberi et al., 2005). At the Galapagos spreading center, high melt flux produces a stacked sill structure similar to the EPR while spreading at intermediate rates of $53\text{--}58\text{ mm/year}$ (Boddupalli & Canales, 2019). We suggest that despite the slow-spreading rates on the EAVS, high melt flux is allowing the presence of shallow axial magma bodies typical of fast-spreading ridges.

5. Conclusions

Erta 'Ale volcano and the EAVS represent the final stage of continental breakup and the development of systems analogous to MORs. We use a time series of Sentinel-1 InSAR observations at Erta 'Ale from October 2014 to June 2019 to study the behavior of the shallow plumbing system in the buildup to and during the long-lived January 2017 eruption. The eruption on the south flank of Erta 'Ale, $\sim 3\text{ km}$ to the SE of the long-lived lava lake, began on 21 January 2017 and produced lava flows that were still active at time of writing (August 2019) (MIROVA, 2019).

In the buildup to the eruption, from October 2014 to January 2017, we observe gradual extension across the ridge axis at a rate of $60 \pm 10\text{ mm/year}$, over 3 times higher than the long-term plate spreading rate at Erta 'Ale. This is consistent with the opening of a $\sim 5 \times 5\text{ km}$ dike at $\sim 500\text{ m}$ depth below the Erta 'Ale summit caldera and eruption site. The lava lake level remains steady at $<20\text{ m}$ below the pit rim during the preeruption period. In order to sustain both the lava lake level and continuous extension, we propose that the magma flux during this time period was at least equal to the rate of dike opening of $0.02\text{--}0.11\text{ m}^3/\text{s}$.

The cointrusive deformation pattern is consistent with a shallow dike intrusion extending from the summit caldera to the eruption site on the south flank of Erta 'Ale and conduit contraction below the summit caldera. Coincident with the initial eruption, we observe a $90 \pm 10\text{ m}$ drop in lava lake level, which was overflowing immediately before the eruption. We find that the pressure loss of $2.5 \pm 0.5\text{ MPa}$ associated with the drop in lava lake level is able to reproduce the observed deformation pattern, indicating that the lava lake is well connected to the shallow plumbing system at Erta 'Ale. The lava lake level is also sensitive to the postintrusion inflation and gradual deflation of a shallow sill at $\sim 1.3\text{ km}$ depth (Xu et al., 2017). From petrological evidence by Field et al. (2012), we suggest that the Erta 'Ale lava lake may be sustained by a shallow reservoir at $\sim 1\text{ km}$ depth.

We do not detect a deeper concentrated magma body below the shallow plumbing system, as is observed elsewhere on the EAVS (Pagli et al., 2012), on Hawaii (e.g., Poland et al., 2014), and at fast-spreading MORs (e.g., Marjanović et al., 2018). Instead, we detect an off-rift deflating vertically extensive source from ~ 1 to 14 km depth, which likely represents a more complex system of smaller stacked sources. We suggest that melt storage at Erta 'Ale may also be distributed throughout the upper crust, with episodes of melt influx forming axial dike structures as observed between 2014–2017 and 2004–2005 (Barnie et al., 2016).

We monitor the area of extruded lava flows using InSAR coherence measurements and establish an eruption rate of 0.4–2.5 m³/s from a period of linear flow area growth between January and November 2017. Over the total post-eruption period, we observe no significant ground deformation, indicating that the rate of eruption is roughly equal to rate of magma flux through the shallow plumbing system at Erta 'Ale. Our estimate of erupted volume up to June 2019 of 12.5–67.5 × 10⁶ m³ is consistent with our modeled co-eruptive sources of deformation, in agreement with a relative increase in extruded material as the EAVS develops through continental breakup (Keir et al., 2013).

Magma plumbing systems at Erta 'Ale and Alu-Dalafilla on the slow-spreading EAVS show features typical of those found at fast-spreading MORs, such as shallow axial magma bodies overlying a system of deeper stacked sills, distributed melt, or a dike-fed structure (Pagli et al., 2012; Wanless & Behn, 2017). We propose that high magma flux on the EAVS may facilitate the development of these shallow bodies on a slow-spreading ridge.

Acknowledgments

All Sentinel-1 data are sourced from the European Union Copernicus Programme. We perform data processing on the JASMIN facility, operated by the Centre for Environmental Data Analysis (CEDA), and postprocessing and figure generation using MATLAB and GMT. This work was funded by the National Environment Research Council (NERC) RiftVolc project (NE/L013649/1) and supported by the Centre for Observation and Modelling of Earthquakes, Volcanoes, and Tectonics (COMET). Data were archived with NERC's National Geoscience Data Centre (NGDC) and can be found online (<https://www.bgs.ac.uk/services/ngdc/accessions/index.html?simpleText=ethiopia>).

References

- Amelung, F., Oppenheimer, C., Segall, P., & Zebker, H. (2000). Ground deformation near Gada 'Ale volcano, Afar, observed by radar interferometry. *Geophysical Research Letters*, 27(19), 3093–3096. <https://doi.org/10.1029/2000GL008497>
- Amelung, F., Yun, S.-H., Walter, T. R., Segall, P., & Kim, S.-W. (2007). Stress control of deep rift intrusion at Mauna Loa Volcano, Hawaii. *Science*, 316(5827), 1026–1030.
- Anderson, K. R., & Poland, M. P. (2016). Bayesian estimation of magma supply, storage, and eruption rates using a multiphysical volcano model: Kīlauea Volcano, 2000–2012. *Earth and Planetary Science Letters*, 447, 161–171.
- Anderson, K. R., Poland, M. P., Johnson, J. H., & Miklius, A. (2015). Episodic deflation-inflation events at Kīlauea Volcano and implications for the shallow magma system. *Hawaiian Volcanoes: From Source to Surface*, 208, 229.
- ArRajehi, A., McClusky, S., Reilinger, R., Daoud, M., Alchalbi, A., Ergintav, S., et al. (2010). Geodetic constraints on present-day motion of the Arabian Plate: Implications for Red Sea and Gulf of Aden rifting. *Tectonics*, 29, TC3011. <https://doi.org/10.1029/2009TC002482>
- Bagnardi, M., & Hooper, A. (2018). Inversion of surface deformation data for rapid estimates of source parameters and uncertainties: A Bayesian approach. *Geochemistry, Geophysics, Geosystems*, 19, 2194–2211. <https://doi.org/10.1029/2018GC007585>
- Bagnardi, M., Poland, M. P., Carbone, D., Baker, S., Battaglia, M., & Amelung, F. (2014). Gravity changes and deformation at Kīlauea Volcano, Hawaii, associated with summit eruptive activity, 2009–2012. *Journal of Geophysical Research: Solid Earth*, 119, 7288–7305. <https://doi.org/10.1002/2014JB011506>
- Barberi, F., & Varet, J. (1970). The Erta Ale volcanic range (Danakil Depression, northern Afar, Ethiopia). *Bulletin Volcanologique*, 34(4), 848–917.
- Barnie, T. D., Oppenheimer, C., & Pagli, C. (2016). Does the lava lake of Erta 'Ale volcano respond to regional magmatic and tectonic events? An investigation using Earth observation data. *Geological Society, London, Special Publications*, 420, 181–208.
- Bastow, I. D., & Keir, D. (2011). The protracted development of the continent-ocean transition in Afar. *Nature Geoscience*, 4(4), 248–250.
- Berardino, P., Fornaro, G., Lanari, R., & Sansosti, E. (2002). A new algorithm for surface deformation monitoring based on small baseline differential SAR interferograms. *IEEE Transactions on Geoscience and Remote Sensing*, 40(11), 2375–2383. <https://doi.org/10.1109/TGRS.2002.803792>
- Bird, P. (2003). An updated digital model of plate boundaries. *Geochemistry, Geophysics, Geosystems*, 4(3), 1027. <https://doi.org/10.1029/2001GC000252>
- Boddupalli, B., & Canales, J. P. (2019). Distribution of crustal melt bodies at the hotspot-influenced section of the Galápagos Spreading Centre from seismic reflection images. *Geophysical Research Letters*, 46, 4664–4673. <https://doi.org/10.1029/2019GL082201>
- Burgi, P.-Y., Darrah, T. H., Tedesco, D., & Eymold, W. K. (2014). Dynamics of the Mount Nyiragongo lava lake. *Journal of Geophysical Research: Solid Earth*, 119, 4106–4122. <https://doi.org/10.1002/2013JB010895>
- Carbotte, S. M., Marjanović, M., Carton, H., Mutter, J. C., Canales, J. P., Nedimović, M. R., et al. (2013). Fine-scale segmentation of the crustal magma reservoir beneath the East Pacific Rise. *Nature Geoscience*, 6(10), 866–870.
- Carn, S. (2019). 12 March. [Online]. [Accessed 15 March 2019]. Available from: <https://twitter.com/simoncarn>
- Dietterich, H. R., Poland, M. P., Schmidt, D. A., Cashman, K. V., Sherrod, D. R., & Espinosa, A. T. (2012). Tracking lava flow emplacement on the east rift zone of Kīlauea, Hawaii, with synthetic aperture radar coherence. *Geochemistry, Geophysics, Geosystems*, 13, Q05001. <https://doi.org/10.1029/2011GC004016>
- Ebinger, C. J. (2005). Continental break-up: The East African perspective. *Astronomy & Geophysics*, 46(2), 2–16.
- Ebinger, C. J., & Casey, M. (2001). Continental breakup in magmatic provinces: An Ethiopian example. *Geology*, 29(6), 527–530.
- Ebinger, C. J., Keir, D., Bastow, I. D., Whaler, K., Hammond, J. O. S., Ayele, A., et al. (2017). Crustal structure of active deformation zones in Africa: Implications for global crustal processes. *Tectonics*, 36, 3298–3332. <https://doi.org/10.1002/2017TC004526>
- Elliott, J. R., Biggs, J., Parsons, B., & Wright, T. J. (2008). InSAR slip rate determination on the Altyn Tagh Fault, northern Tibet, in the presence of topographically correlated atmospheric delays. *Geophysical Research Letters*, 35, L12309. <https://doi.org/10.1029/2008GL033659>
- Farr, T. G., & Kobrick, M. (2000). Shuttle Radar Topography Mission produces a wealth of data. *Eos, Transactions American Geophysical Union*, 81(48), 583–585.
- Field, L., Barnie, T., Blundy, J., Brooker, R. A., Keir, D., Lewi, E., & Saunders, K. (2012). Integrated field, satellite and petrological observations of the November 2010 eruption of Erta Ale. *Bulletin of Volcanology*, 74, 2251–2271.
- Gerlach, T. M. (1980). Investigation of volcanic gas analyses and magma outgassing from Erta'Ale lava lake, Afar, Ethiopia. *Journal of Volcanology and Geothermal Research*, 7(3–4), 415–441.
- Global Volcanism Program (2017). Report on Erta Ale (Ethiopia). In S. K. Sennert (Ed.), *Weekly volcanic activity report*: Smithsonian Institution and US Geological Survey. 25 January–31 January 2017.
- Global Volcanism Program (2018). Report on Erta Ale (Ethiopia). In E. Venzke (Ed.), *Bulletin of the Global Volcanism Network*: Smithsonian Institution. 43:4. <https://doi.org/10.5479/si.GVP.BGVN201804-221080>

- González, P. J., Walters, R. J., Hatton, E. L., Spaans, K., & Hooper, A. (2016). LiCSAR: Tools for automated generation of Sentinel-1 frame interferograms. AGU Fall Meeting.
- Hamling, I. J., Wright, T. J., Calais, E., Lewi, E., & Fukahata, Y. (2014). InSAR observations of post-rifting deformation around the Dabbahu rift segment, Afar, Ethiopia. *Geophysical Journal International*, *197*, 33–49. <https://doi.org/10.1093/gji/ggu003>
- Hammond, J. O. S., Kendall, J. M., Stuart, G. W., Keir, D., Ebinger, C., Ayele, A., & Belachew, M. (2011). The nature of the crust beneath the Afar triple junction: Evidence from receiver functions. *Geochemistry, Geophysics, Geosystems*, *12*, Q12004. <https://doi.org/10.1029/2011GC003738>
- Hayward, N. J., & Ebinger, C. J. (1996). Variations in the along-axis segmentation of the Afar rift system. *Tectonics*, *15*(2), 244–257.
- Hooper, A., Segall, P., Johnson, K., & Rubinstein, J. (2002). Reconciling seismic and geodetic models of the 1989 Kilauea south flank earthquake. *Geophysical Research Letters*, *29*(22), 2062.
- Hutchison, W., Mather, T. A., Pyle, D. M., Boyce, A. J., Gleeson, M. L., Yirgu, G., & Finch, A. A. (2018). The evolution of magma during continental rifting: New constraints from the isotopic and trace element signatures of silicic magmas from Ethiopian volcanoes. *Earth and Planetary Science Letters*, *489*, 203–218. <https://doi.org/10.1016/j.epsl.2018.02.027>
- Illsley-Kemp, F., Bull, J., Keir, D., Gerya, T., Pagli, C., Gernon, T., et al. (2018b). Initiation of a proto-transform fault prior to seafloor spreading. *Geochemistry, Geophysics, Geosystems*, *19*, 4744–4756. <https://doi.org/10.1029/2018GC007947>
- Illsley-Kemp, F., Keir, D., Bull, J. M., Gernon, T. M., Ebinger, C., Ayele, A., et al. (2018a). Seismicity during continental breakup in the Red Sea rift of Northern Afar. *Journal of Geophysical Research: Solid Earth*, *123*, 2345–2362. <https://doi.org/10.1002/2017JB014902>
- Jones, L. K., Kyle, P. R., Oppenheimer, C., Frechette, J. D., & Okal, M. H. (2015). Terrestrial laser scanning observations of geomorphic changes and varying lava lake levels at Erebus volcano, Antarctica. *Journal of Volcanology and Geothermal Research*, *295*, 43–54.
- Jónsson, S., Zebker, H., Segall, P., & Amelung, F. (2002). Fault slip distribution of the 1999 Mw 7.1 Hector Mine, California, earthquake, estimates from satellite radar and GPS measurements. *Bulletin of the Seismological Society of America*, *92*(4), 1377–1389.
- Keir, D., Bastow, I. D., Pagli, C., & Chambers, E. L. (2013). The development of extension and magmatism in the Red Sea rift of Afar. *Tectonophysics*, *607*, 98–114.
- Lanari, R., Casu, F., Manzo, M., Zeni, G., Berardino, P., Manunta, M., & Pepe, A. (2007). An overview of the small baseline subset algorithm: A DInSAR technique for surface deformation analysis. *Pure and Applied Geophysics*, *164*(4), 637–661. <https://doi.org/10.1007/s00024-007-0192-9>
- Lanari, R., Mora, O., Manunta, M., Mallorqui, J., Berardino, P., & Sansosti, E. (2004). A small baseline approach for investigating deformations on full resolution differential SAR interferograms. *IEEE Transactions on Geoscience and Remote Sensing*, *42*(7), 1377–1386.
- Le Guern, F., Carbonnelle, J., & Tazieff, H. (1979). Erta'Ale lava lake: Heat and gas transfer to the atmosphere. *Journal of Volcanology and Geothermal Research*, *6*, 27–48.
- MIROVA (2019). Middle InfraRed Observation of Volcanic Activity (MIROVA): Erta Ale. [Online]. [Accessed 03 July 2019]. Available from: www.mirovaweb.it
- Marjanović, M., Carbotte, S. M., Carton, H. D., Nedimović, M. R., Canales, J. P., & Mutter, J. C. (2018). Crustal magmatic system beneath the East Pacific Rise (8°20' to 10°10' N): Implications for tectonomagmatic segmentation and crustal melt transport at fast-spreading ridges. *Geochemistry, Geophysics, Geosystems*, *19*, 4584–4611. <https://doi.org/10.1029/2018GC007590>
- Marjanović, M., Carbotte, S. M., Carton, H., Nedimović, M. R., Mutter, J. C., & Canales, J. P. (2014). A multi-sill magma plumbing system beneath the axis of the East Pacific Rise. *Nature Geoscience*, *7*(11), 825.
- Massonnet, D., & Feigl, K. L. (1998). Radar interferometry and its application to changes in the Earth's surface. *Reviews of Geophysics*, *36*(4), 441–500.
- McClusky, S., Reilinger, R., Ogubazghi, G., Amleson, A., Healeb, B., Vernant, P., et al. (2010). Kinematics of the southern Red Sea-Afar Triple Junction and implications for plate dynamics. *Geophysical Research Letters*, *37*, L05301. <https://doi.org/10.1029/2009GL041127>
- Montagna, C. P., & Gonnermann, H. M. (2013). Magma flow between summit and Pu'u'u'ūōō at Kilauea Volcano, Hawaii. *Geochemistry, Geophysics, Geosystems*, *14*, 2232–2246. <https://doi.org/10.1002/ggge.20145>
- Moussallam, Y., Bani, P., Curtis, A., Barnie, T., Moussallam, M., Peters, N., et al. (2016). Sustaining persistent lava lakes: Observations from high-resolution gas measurements at Villarrica Volcano, Chile. *Earth and Planetary Science Letters*, *454*, 237–247.
- Neal, C., Brantley, S., Antolik, L., Babb, J., Burgess, M., Calles, K., et al. (2019). The 2018 rift eruption and summit collapse of Kilauea Volcano. *Science*, *363*(6425), 367–374.
- Nobile, A., Pagli, C., Keir, D., Wright, T. J., Ayele, A., Ruch, J., & Acocella, V. (2012). Dike-fault interaction during the 2004 Dallo intrusion at the northern edge of the Erta Ale Ridge (Afar, Ethiopia). *Geophysical Research Letters*, *39*, L19305. <https://doi.org/10.1029/2012GL053152>
- Okada, Y. (1985). Surface deformation due to shear and tensile faults in a half-space. *Bulletin of the seismological society of America*, *75*(4), 1135–1154.
- Oppenheimer, C., Lomakina, A. S., Kyle, P. R., Kingsbury, N. G., & Boichu, M. (2009). Pulsatory magma supply to a phonolite lava lake. *Earth and Planetary Science Letters*, *284*(3), 392–398.
- Pagli, C., Wang, H., Wright, T. J., Calais, E., & Lewi, E. (2014). Current plate boundary deformation of the Afar rift from a 3-D velocity field inversion of InSAR and GPS. *Journal of Geophysical Research: Solid Earth*, *119*, 8562–8575. <https://doi.org/10.1002/2014JB011391>
- Pagli, C., Wright, T. J., Ebinger, C. J., Yun, S. H., Cann, J. R., Barnie, T., & Ayele, A. (2012). Shallow axial magma chamber at the slow-spreading Erta Ale Ridge. *Nature Geoscience*, *5*(4), 284–288.
- Patrick, M., Anderson, K., Poland, M., Orr, T., & Swanson, D. (2015). Lava lake level as a gauge of magma reservoir pressure and eruptive hazard. *Geology*, *43*(9), 831–834.
- Patrick, M., Orr, T., Anderson, K., & Swanson, D. (2019a). Eruptions in sync: Improved constraints on Kilauea Volcano's hydraulic connection. *Earth and Planetary Science Letters*, *507*, 50–61.
- Patrick, M., Swanson, D., & Orr, T. (2019b). A review of controls on lava lake level: Insights from Halema'uma'u Crater, Kilauea Volcano. *Bulletin of Volcanology*, *81*(3), 13.
- Poland, M. P., & Carbone, D. (2018). Continuous gravity and tilt reveal anomalous pressure and density changes associated with gas pistonning within the summit lava lake of Kilauea Volcano, Hawai'i. *Geophysical Research Letters*, *45*, 2319–2327. <https://doi.org/10.1002/2017GL076936>
- Poland, M. P., Miklius, A., & Montgomery-Brown, E. K. (2014). Magma supply, storage, and transport at shield-stage Hawaiian volcanoes. *Characteristics of Hawaiian Volcanoes*, *179*(1801), 179–234.
- Rivalta, E., & Segall, P. (2008). Magma compressibility and the missing source for some dike intrusions. *Geophysical Research Letters*, *35*, L04306. <https://doi.org/10.1029/2007GL032521>
- Rosen, P. A., Hensley, S., Zebker, H. A., Webb, F. H., & Fielding, J. E. (1996). Surface deformation and coherence measurements of Kilauea Volcano, Hawaii, from SIR-C radar interferometry. *Journal of Geophysical Research*, *101*(E10), 23,109–23,125.

- Shreve, T., Grandin, R., Boichu, M., Garaebiti, E., Moussallam, Y., Ballu, V., et al. (2019). From major caldera subsidence to quiescence at the world's top volcanic degassing source, Ambrym, Vanuatu: The influence of regional tectonics. *EarthArXiv*, <https://doi.org/10.31223/osf.io/c8d5v>
- Sigmundsson, F. (2016). New insights into magma plumbing along rift systems from detailed observations of eruptive behavior at Axial volcano. *Geophysical Research Letters*, *43*, 12,423–12,427. <https://doi.org/10.1002/2016GL071884>
- Tiberi, C., Ebinger, C., Ballu, V., Stuart, G., & Oluma, B. (2005). Inverse models of gravity data from the Red Sea-Aden-East African rifts triple junction zone. *Geophysical Journal International*, *163*, 775–787.
- Varet, J. (1971). Erta'Ale activity (Afar, Ethiopia). *Bulletin of the Geophysical Observatory, Addis Ababa*, *13*, 115–119.
- Volcano Discovery (2017). Erta Ale (Ethiopia) volcano news. [Online]. [Accessed 15 March 2019]. Available from: www.volcanodiscovery.com/erta_ale/news.html
- Wadge, G., Biggs, J., Lloyd, R., & Kendall, J.-M. (2016). Historical Volcanism and the state of stress in the East African Rift System. *Frontiers in Earth Science*, *4*(86), 1–24.
- Wanless, V. D., & Behn, M. D. (2017). Spreading rate-dependent variations in crystallization along the global mid-ocean ridge system. *Geochemistry, Geophysics, Geosystems*, *18*, 3016–3033. <https://doi.org/10.1002/2017GC006924>
- Werner, C., Wegmuller, U., Strozzi, T., & Wiesmann, A. (2000). GAMMA SAR and interferometric processing software. *European Space Agency, (Special Publication) ESA SP*, *461*, 211–219.
- Wolfenden, E., Ebinger, C., Yirgu, G., Renne, P. R., & Kelley, S. P. (2005). Evolution of a volcanic rifted margin: Southern Red Sea, Ethiopia. *Bulletin of the Geological Society of America*, *117*(7/8), 846–864.
- Wright, T. J., Parsons, B. E., & Zhong, L. (2004). Toward mapping surface deformation in three dimensions using InSAR. *Geophysical Research Letters*, *31*, L01607. <https://doi.org/10.1029/2003GL018827>
- Wright, T. J., Sigmundsson, F., Pagli, C., Belachew, M., Hamling, I. J., Brandsdóttir, B., et al. (2012). Geophysical constraints on the dynamics of spreading centres from rifting episodes on land. *Nature Geoscience*, *5*(4), 242–250.
- Xu, W., Rivalta, E., & Li, X. (2017). Magmatic architecture within a rift segment: Articulate axial magma storage at Erta Ale volcano, Ethiopia. *Earth and Planetary Science Letters*, *476*, 79–86.
- Yang, X.-M., Davis, P. M., & Dieterich, J. H. (1988). Deformation from inflation of a dipping finite prolate spheroid in an elastic half-space as a model for volcanic stressing. *Journal of Geophysical Research*, *93*(B5), 4249–4257.
- Yu, C., Li, Z., & Penna, N. T. (2018). Interferometric synthetic aperture radar atmospheric correction using a GPS-based iterative tropospheric decomposition model. *Remote Sensing of Environment*, *204*, 109–121.
- Yu, C., Penna, N. T., & Li, Z. (2017). Generation of real-time mode high-resolution water vapor fields from GPS observations. *Journal of Geophysical Research: Atmospheres*, *122*, 2008–2025. <https://doi.org/10.1002/2016JD025753>